Autophagy adaptors mediate Parkin-dependent mitophagy by forming sheet-like liquid condensates

Zi Yang[1], Saori R. Yoshii[1], Yuji Sakai[1,2,3], Haruka Chino[1], Roland L. Knorr[1,4,5], Noboru Mizushima[1,6*]

[1]Department of Biochemistry and Molecular Biology, Graduate School of Medicine, The University of Tokyo, Tokyo, Japan.

[2]Department of Biosystems Science, Institute for Life and Medical Sciences, Kyoto University, Sakyo-ku, Kyoto 606-8507, Japan

[3]Interdisciplinary Theoretical and Mathematical Sciences (iTHEMS) Program, RIKEN, Wako, Saitama 351-0198, Japan

[4]Institute of Biology, Humboldt-Universität zu Berlin, Berlin, Germany

[5]International Research Frontiers Initiative, Institute of Innovative Research, Tokyo Institute of Technology

[6]International Research Center for Neurointelligence (WPI-IRCN), UTIAS, The University of Tokyo, Tokyo 113-8655, Japan

*Corresponding author. Department of Biochemistry and Molecular Biology, Graduate School of Medicine, The University of Tokyo, 7-3-1 Hongo, Bunkyo-ku, Tokyo 113-0033, Japan; Tel: +81-3-5841-3440; Fax: +81-3-3815-1490; E-mail: nmizu@m.u-tokyo.ac.jp

Abstract

During PINK1 and Parkin-mediated mitophagy, autophagy adaptors are recruited to depolarized mitochondria to promote the selective degradation of mitochondria. Autophagy adaptors such as OPTN and NDP52 bridge mitochondria and autophagosomal membranes by binding to ubiquitinated mitochondrial proteins and autophagosomal ATG8 family proteins. Here, we demonstrate that OPTN and NDP52 form sheet-like phase-separated condensates with liquid-like properties on the surface of ubiquitinated mitochondria. The dynamic and liquid-like feature of OPTN condensates is important for mitophagy activity because reducing the liquidity of OPTN–ubiquitin condensates suppresses the recruitment of ATG9 vesicles and impairs mitophagy. Based on these results, we propose a dynamic liquid-like model of autophagy adaptors, in contrast to a stoichiometric model, to explain their interactions between autophagic membranes (i.e., ATG9 vesicles and isolation membranes) and mitochondrial membranes during Parkin-mediated mitophagy. This model underscores the importance of liquid–liquid phase separation in facilitating membrane–membrane contacts, likely through the generation of capillary forces.

Keywords

autophagy; mitophagy; liquid–liquid phase separation; optineurin; wetting

Introduction

Macroautophagy (hereafter referred to as autophagy) is an intracellular degradation process mediated by a double-membraned organelle termed the autophagosome (Nakatogawa, 2020; Mizushima & Levine, 2020). Cytosolic components such as proteins and organelles are segregated into autophagosomes, which subsequently fuse with lysosomes for degradation. Autophagy can be either non-selective or selective (Lamark & Johansen, 2021; Vargas *et al*, 2023). Mitophagy, which is a selective type of autophagy, specifically degrades mitochondria and can be induced by mitochondrial damage or cellular stresses (Onishi *et al*, 2021; Ganley & Simonsen, 2022). For example, after losing the mitochondrial membrane potential, numerous mitochondrial outer-membrane proteins are ubiquitinated by the PINK1-Parkin system, initiating the recruitment of autophagy adaptors, including optineurin (OPTN), calcium binding and coiled-coil domain 2 (CALCOCO2/NDP52), sequestosome 1 (SQSTM1/p62), Next to BRCA1 gene 1 protein (NBR1), and Tax1 binding protein 1 (TAX1BP1) (Lamark & Johansen, 2021; Vargas *et al*, 2023). These autophagy adaptors bridge the mitochondrial and autophagosomal membranes by interacting with mitochondrial ubiquitinated proteins via a ubiquitin-binding domain (UBD) and with autophagosomal ATG8 family proteins (i.e., LC3 and GABARAP family proteins in mammals) via the LC3-interacting region (LIR). In addition to their role in bridging mitochondria and autophagosomes, OTPN and NDP52 also play crucial roles in inducing mitophagy by recruiting upstream autophagy factors (Lazarou *et al*, 2015); OPTN recruits ATG9 vesicles, whereas NDP52 recruits the ULK1 complex through interaction with FIP200 (Yamano *et al*, 2020; Vargas *et al*, 2023).

Liquid–liquid phase separation (LLPS) has been described in various biological processes (Musacchio, 2022; Hirose *et al*, 2023). LLPS involves the formation of liquid-like condensates through dynamic, multivalent interactions between various molecules that often possess intrinsically disordered regions. Emerging evidence suggests connections between autophagy and LLPS at multiple steps, including autophagosome formation and degradation (Noda *et al*, 2020; Ma *et al*, 2023). Notably, autophagy adaptors, such as p62,

69 undergo LLPS through multivalent interaction with poly-ubiquitins and form cytosolic
70 condensates (Zaffagnini *et al*, 2018; Sun *et al*, 2018). These condensates can be degraded
71 by autophagy, which is termed “fluidophagy” (Agudo-Canalejo *et al*, 2021). Furthermore,
72 recent studies showed that p62 undergoes LLPS on mitochondria and lysosomes that are
73 subjected to selective autophagy (Peng *et al*, 2021; Gallagher & Holzbaur, 2023).
74 Generally, phase-separated condensates can deform when they contact a rigid surface
75 in order to minimize the overall energy of the system, a phenomenon known as “wetting”
76 (Kusumaatmaja *et al*, 2021b; Gouveia *et al*, 2022). The wetting behavior of intracellular
77 condensates is determined by the interfacial tensions between the condensate–membrane,
78 condensate–cytosol, and cytosol-membrane interfaces. Depending on the relative
79 strengths of these interfacial tensions, the condensates exhibit partial wetting, complete
80 wetting, or de-wetting. In contrast, elastic surfaces, including membranes to which phase-
81 separated condensates adhere, also deform (Kusumaatmaja *et al*, 2021a, 2021b; Gouveia
82 *et al*, 2022). This indeed happens during fluidophagy; autophagosomal membranes bend
83 along the surface of p62 condensates (Agudo-Canalejo *et al*, 2021). Deformation of a
84 membrane by a phase-separated condensate is determined by the energy balance
85 between membrane deformation and the surface tension of the condensate, which is
86 known as elastocapillarity (Style *et al*, 2017; Kusumaatmaja *et al*, 2021b).
87 By forming capillary bridges, wetting droplets can also induce adhesion of surfaces
88 (Wexler *et al*, 2014). Whether LLPS and capillary bridges also contribute to the adhesion of
89 cellular membranes is not presently known. Therefore, we hypothesized that phase-
90 separated condensates of autophagy adaptors can wet both mitochondria and autophagic
91 membranes, including ATG9 vesicles and isolation membranes (also called phagophores),
92 thereby promoting their contact during Parkin-mediated mitophagy. In this study, we employ
93 live-cell imaging and a mathematical model to provide evidence that the autophagy
94 adaptors form phase-separated condensates on the surface of the mitochondrial
95 membrane, resulting in sheet-like condensates that cover the surface of ubiquitinated
96 mitochondria upon mitophagy induction. These condensates accumulate between

mitochondria or between mitochondria and autophagic membranes, exhibiting a dynamic nature with a liquid-like property. Furthermore, we demonstrate the essential role of these dynamic condensates in the recruitment of ATG9 vesicles and the initiation of mitophagy. Based on these results, we propose a dynamic liquid-like model, rather than a stoichiometric model, to describe the roles of autophagy adaptors in Parkin-mediated mitophagy.

Results

Autophagy adaptors show distinct distributions during Parkin-mediated mitophagy

To better understand the role of each autophagy adaptor, we analyzed their localization during Parkin-mediated mitophagy. When mitophagy was induced by treatment with the mitochondrial uncoupler carbonyl cyanide *m*-chlorophenylhydrazone (CCCP) in HeLa cells expressing exogenous Parkin, the autophagy adaptors p62, OPTN, NBR1, NDP52, and TAX1BP1 translocated to mitochondria as previously observed (Fig. 1A and B) (Geisler *et al*, 2010; Wong & Holzbaur, 2014; Heo *et al*, 2015; Moore & Holzbaur, 2016; Gallagher & Holzbaur, 2023). Ubiquitin and all of these autophagy adaptors were distributed evenly on the surface of separate mitochondria (Mt; Fig. 1A). In contrast, these adaptors exhibited distinct localization patterns during the formation of isolation membranes on mitochondria (Mt–IM; Fig. 1B and C). The signals of OPTN and NDP52 were enriched in areas where LC3B signals colocalized, while they were mostly absent from the LC3B-negative side of the same mitochondria (Fig. 1B and C). Endogenous OPTN and NDP52 also showed clear enrichment on the LC3B-positive areas in comparison to the LC3B-negative side, confirming that this localization is not caused by the overexpression of adaptors (Fig. 1D). However, this inhomogeneous distribution pattern was not observed for ubiquitin, p62, NBR1, and TAX1BP1 (Fig. 1B and C). Unlike OPTN and NDP52, p62 showed enrichment between clustered mitochondria (Mt-Mt), which is consistent with previous reports (Fig. EV1A and B) (Wong & Holzbaur, 2014). These accumulation patterns cannot be explained by the stoichiometric interaction of the autophagy adaptors with ubiquitinated proteins that are evenly distributed on mitochondria.

The localization of autophagy adaptors may be affected by their interaction with other adaptors (Turco *et al*, 2021; Gubas & Dikic, 2022). To examine the localization of each adaptor on its own, we used HeLa cells lacking all five autophagy adaptors (penta KO cells) to exclude the effect of other adaptors (Lazarou *et al*, 2015). In penta KO cells, OPTN and NDP52 exhibited significant enrichment in LC3B-positive areas, similar to that observed in

132 wild-type cells, suggesting that this accumulation occurred independently of heterologous
133 interaction with other adaptors (Fig. 1E and F). Mitophagy was not restored by exogenous
134 expression of p62 or NBR1 in penta KO cells, and thus colocalization with LC3 could not be
135 tested for these two adaptors (Lazarou *et al*, 2015). The accumulation of p62 between
136 clustered mitochondria was also observed in penta KO cells (Fig. EV1C and D). Given the
137 uniform distribution of ubiquitinated proteins on mitochondrial surfaces, these data suggest
138 that autophagy adaptors exhibit non-stoichiometric enrichment between membranes.
139 Hereafter, we used penta KO cells to study each autophagy adapter individually
140

141 **OPTN and NDP52 show a dynamic exchange between the mitochondrial surface and**
142 **cytosol**

143 We hypothesized that the non-stoichiometric distribution of the autophagy adaptors on
144 ubiquitinated mitochondria could be explained by LLPS. Typical condensates generated by
145 LLPS exhibit rapid exchange of their components, which is often demonstrated by
146 fluorescence recovery after photobleaching (FRAP) analysis (Taylor *et al*, 2019;
147 McSwiggen *et al*, 2019). We first conducted FRAP experiments for separate (i.e.,
148 unclustered) mitochondria in CCCP-treated cells. As expected, ubiquitin showed virtually no
149 recovery because it was conjugated to mitochondrial membrane proteins (Fig. 2A and B).
150 Additionally, p62 recovered only slightly, suggesting a minute exchange between the
151 mitochondrial surface and cytosol (Fig. 2A and B). In contrast, OPTN and NDP52 showed a
152 rapid recovery, indicating a dynamic exchange of these adaptors between the mitochondrial
153 surface and the cytosol (Fig. 2A and B).

154 Next, we examined the dynamics of adaptors between mitochondria and isolation
155 membranes. OPTN and NDP52 showed partial recovery (Fig. 2C and D). Although this
156 result indicates some exchange of these adaptors between membranes, the incomplete
157 recovery suggests the existence of a gel-like or immobile fraction. Treatment with 1,6-
158 hexanediol, which can be used to dissolve condensates, dispersed OPTN from
159 mitochondria without isolation membranes, suggesting that OPTN accumulation is

160 supported by weak interactions (Fig. 2E). These results indicate that OPTN and NDP52 on
161 ubiquitinated mitochondria are mobile and can quickly exchange between the mitochondrial
162 surface and the cytosol, supporting the hypothesis that they form phase-separated
163 condensates on damaged mitochondria.
164
165 **Mathematical models of condensate formation and localization of autophagy**
166 **adaptors**
167 To simulate the behavior of autophagy adaptors in the context of phase-separated
168 condensates, we developed mathematical models (see Materials and Methods for details).
169 First, we considered the case of two mitochondria approaching each other (Fig. 3A). In
170 Parkin-mediated mitophagy, various proteins in the mitochondrial outer membrane are
171 ubiquitinated. We modeled the mitochondrial outer membrane as a circle with a diameter of
172 $D_{Mt} = 600$ nm. On these mitochondria, we assumed a ring-shaped ubiquitin layer with a
173 thickness $w_{Ub} = 20$ nm and area-fraction (hereafter referred to as concentration) $\phi_{Ub} = 0.1$
174 (Milo & Phillips, 2015; Berry *et al*, 2018) (Fig. 3A). The closest distance between the two
175 mitochondrial outer membranes was set to d_{Mt} (Fig. 3A). Here, we considered the
176 dynamics of concentration changes of the adapter proteins and solvent components. We
177 assumed that mitochondria were very large compared with proteins and did not move on a
178 similarly short time scale, and that ubiquitin was tightly bound to mitochondrial membranes
179 and immobile, as suggested by the FRAP experiment (Fig. 2B). The adaptor proteins were
180 assumed to diffuse freely in solution and to bind to ubiquitin and themselves (self-
181 interactions) with strengths χ_{Ub} and χ_{self}, respectively.
182 Using the mathematical model, we assessed how the condensates deformed when the
183 distance between two mitochondria d_{Mt} was changed, where $\chi_{Ub} = 12k_BT$ and $\chi_{self} =$
184 $3k_BT$, with the Boltzmann constant k_B and temperature T. When two mitochondria were far
185 apart ($d_{Mt} = 900$ nm), the model predicted that adaptors cover the entire mitochondrial
186 surface (Fig. 3B). When the mitochondria were close enough to come into contact ($d_{Mt} =$
187 60 nm), the adaptors moved to the area between the mitochondria and filled the cleft

188 between them (arrowheads, Fig. 3B).

189 Next, we considered the case in which a growing isolation membrane surrounded and
190 enclosed a single mitochondrion (Fig. 3C and D). A mitochondrion with ubiquitin was
191 modeled as mentioned above, and the isolation membrane was modeled as a region of
192 thickness $w_{IM} = 50$ nm bound by two semicircles with the same center as the
193 mitochondrion. The closest distance between the isolation membrane and the
194 mitochondrial outer membrane was $d_{IM} = 100$ nm, and the isolation membrane bent at an
195 angle α to surround the mitochondrion. The surface of the isolation membrane was
196 assumed to be covered by an LC3 region with a thickness $w_{LC3} = 20$ nm and concentration
197 $\phi_{LC3} = 0.1$. The adaptors interacted with both LC3 and ubiquitin with strengths χ_{LC3} and
198 χ_{Ub}, respectively.

199 Using this model, we determined the distribution of the adaptors when the isolation
200 membrane appeared and elongated (changing the angle α surrounding the mitochondrion).
201 The interaction strengths were set to $\chi_{Ub} = \chi_{LC3} = 12k_BT$ and $\chi_{self} = 3k_BT$. In the absence
202 of the isolation membrane, the adaptors wet the entire mitochondrial surface uniformly (Fig.
203 3D). However, with the appearance of the isolation membrane, the adaptors remobilized to
204 the area between the isolation membrane and mitochondrion, and this adaptor-enriched
205 region elongated together with the isolation membrane. These modeling results suggest
206 that the distribution of the adaptors on a mitochondrion can change upon contact with
207 another mitochondrion or an isolation membrane.

208

209 **OPTN condensates redistribute upon membrane contact**

210 Our mathematical models predict that the OPTN distribution changes when mitochondria
211 cluster or are engulfed by isolation membranes. We then validated these predictions by
212 using live-cell imaging. When two small mitochondria with uniform OPTN distributions on
213 their surface approached each other, OPTN redistributed and formed a smooth surface that
214 covered the two adjacent mitochondria (Fig. 4A–D, Movie EV1). Notably, strong OPTN
215 enrichment was observed in the cleft between the two mitochondria (arrowheads, Fig. 4A

216 and C), showing a pattern distinct from that of the outer membrane protein Omp25 (OPTN
217 signal peaks localized outside of Omp25 signal peaks) (Fig. 4B and D). This phenomenon
218 was apparent when the size of both (Fig. 4A) or one (Fig. 4C, Movie EV1) of the two
219 mitochondria was less than 1 μm. Although OPTN formed sheet-like rather than spherical
220 condensates, this phenomenon appeared to be similar to condensate coalescence, which
221 is one of the hallmarks of liquid-like condensates (Hyman *et al*, 2014).
222 Furthermore, when an isolation membrane started to engulf a mitochondrion, OPTN,
223 which was initially distributed uniformly on the mitochondrial surface, underwent
224 redistribution to the area contacting the isolation membrane (Fig. 4E, Movie EV2). OPTN
225 signals on the isolation membrane-negative side of the mitochondrion diminished during
226 this process (Fig. 4E and F). The OPTN-enriched region expanded together with the
227 isolation membrane thereafter (Fig. 4E). These live-cell observations are consistent with
228 the predictions of our mathematical models (Fig. 3). Taken together, our experimental data
229 support the hypothesis that OPTN forms sheet-like phase-separated condensates on the
230 surface of ubiquitinated mitochondria, exhibiting liquid-like properties.
231
232 **Liquid-like property of OPTN condensates is required for mitophagy**
233 To investigate the importance of the liquid-like nature of OPTN condensates on
234 mitochondria, we sought to reduce its liquidity by strengthening the interaction but reducing
235 the multivalency between ubiquitin and GFP–OPTN constructs. To achieve this, we utilized
236 the anti-green fluorescent protein (GFP) nanobody, which exhibits a high binding affinity to
237 GFP (Rothbauer *et al*, 2008). Fusing the anti-GFP nanobody to the N-terminus of ubiquitin
238 (nanobody–mRuby–Ub) (Fig. 5A, bottom panel) resulted in significantly enhanced binding
239 to GFP–OPTN (Fig. 5B). Deleting the ubiquitin-binding domain in ABINs and NEMO (UBAN
240 domain) from OPTN (GFP–OPTNΔUBAN) eliminated the interaction with ubiquitinated
241 proteins (Fig. 5B). Wild-type GFP–OPTN accumulated on ubiquitinated mitochondria, but
242 GFP–OPTNΔUBAN failed to do so (Fig. 5A, top and middle panels). In contrast, the
243 expression of nanobody–mRuby–Ub rescued the recruitment of GFP–OPTNΔUBAN to

244 mitochondria (Fig. 5A, lower panel). FRAP experiments revealed that, compared with wild-
245 type GFP–OPTN (with mRuby–Ub, not nanobody-mRuby–Ub), GFP–OPTNΔUBAN
246 showed a substantial decrease in recovery on mitochondria when co-expressed with
247 nanobody–mRuby–Ub, indicating a reduction in its dynamic properties (Fig. 5C).
248 We then evaluated the effect of impaired OPTN liquidity on mitophagy using the
249 recently developed HaloTag cleavage assay (Yim *et al*, 2022). This assay utilizes the
250 ligand-dependent conformational change of HaloTag (Halo); ligand-free Halo is efficiently
251 degraded in lysosomes, whereas ligand-bound Halo becomes resistant to lysosomal
252 degradation. When Halo is expressed in the mitochondrial matrix by fusing to the
253 mitochondrial presequence of Fo-ATPase subunit 9 and SNAP-tag (mtHalo–SNAP), we
254 can measure the extent of mitochondrial degradation by quantifying the amount of
255 processed free Halo out of the total amount of Halo (mtHalo–SNAP + processed Halo).
256 Mitophagy activity, which was impaired in penta KO cells, was restored by the expression
257 of GFP–OPTN (Fig. 5D and E). However, GFP–OPTNΔUBAN failed to restore mitophagy,
258 even when it was co-expressed with nanobody–mRuby–Ub to rescue ubiquitin binding and
259 mitochondrial localization (Fig. 5A, B, D, and E). These data suggest that the localization of
260 OPTN on mitochondria and its binding to ubiquitin alone is insufficient for mitophagy, and
261 the liquidity of OPTN is important for effective mitophagy.
262
263 **Liquid-like property of OPTN condensates is required for the recruitment of ATG9**
264 **vesicles**
265 ATG9 vesicles are considered to be one of the sources of autophagosomal membranes
266 (Yamamoto *et al*, 2012). Upon mitophagy induction, ATG9 vesicles accumulate at the sites
267 of autophagosome formation (Itakura *et al*, 2012). OPTN plays a crucial role in this process
268 by recruiting ATG9 vesicles to induce mitophagy (Yamano *et al*, 2020). In general, liquid-
269 like condensates can be involved in clustering small vesicles such as synaptic vesicles,
270 which exemplify complete wetting (Milovanovic & De Camilli, 2017; Sansevrino *et al*, 2023).
271 Indeed, ATG9 vesicles are incorporated into condensates containing a glaucoma-

associated OPTN mutant (O'Loughlin *et al*, 2020) and synapsin (Park *et al*, 2023). We, therefore, hypothesized that the liquid-like properties of OPTN condensates on mitochondria facilitate the recruitment of ATG9 vesicles. Consistent with previous reports (Itakura *et al*, 2012; Yamano *et al*, 2020), ATG9A was recruited to depolarized mitochondria in cells expressing GFP–OPTN (Fig. 6A and B). However, this ATG9A recruitment was almost completely abolished in cells expressing nanobody–mRuby–Ub and GFP–OPTNΔUBAN (Fig. 6A and B), even though GFP–OPTNΔUBAN still retains the ATG9A-interacting domain and the ability to bind with the ATG9 vesicles (Fig. 6C and D). Taken together, these findings suggest that the liquidity of sheet-like OPTN condensates on the mitochondrial surface is crucial for recruiting ATG9 vesicles and executing mitophagy.

Discussion

LLPS by autophagy adaptors during Parkin-mediated mitophagy

In the present study, we discovered that autophagy adaptors accumulate on ubiquitinated mitochondria with non-stoichiometric distribution compared with ubiquitin signals. They displayed characteristics consistent with phase-separated structures, including dynamic exchange with cytosol and redistribution upon coalescence. Notably, we observed the enrichment of OPTN at the isolation membrane-positive region, which expanded along with the elongation of the isolation membrane. These findings suggest that phase-separated adaptors facilitate the effective engulfment of mitochondria by the isolation membrane through the wetting effect and capillary forces (Fig. 6E, right panel). Moreover, the liquidity of OPTN condensates is critical for the localization of ATG9 vesicles onto ubiquitinated mitochondria, indicating that partial or complete wetting of phase-separated adaptors to ATG9 vesicles may be crucial for their recruitment to and/or retention on mitochondria (Fig. 6E, left panel). Therefore, we propose that LLPS of autophagy adaptors plays a critical role in two distinct steps of mitophagy by producing capillary forces, first, at the initiation step by recruiting and retaining the ATG9 vesicles in the condensates and, second, at the autophagosome elongation step by facilitating the attachment between ubiquitinated mitochondria and the isolation membrane.

LLPS in bulk and selective autophagy

Recent reports have shed light on the importance of LLPS in selective autophagy (Noda *et al*, 2020). In lysophagy, p62 undergoes LLPS on lysosomes to facilitate efficient lysophagy together with HSP27, which maintains the liquidity of p62 and prevents its gelation (Gallagher & Holzbaur, 2023). This may also be mediated by the wetting between damaged lysosomes and the isolation membrane by phase-separated p62. Indeed, p62 itself forms phase-separated condensates along with ubiquitinated proteins, producing capillary forces by the wetting effect to facilitate the engulfment by the isolation membrane (Agudo-

311 Canalejo *et al*, 2021). Similarly, Ape1, the cargo of the cytosol-to-vacuole targeting (Cvt)
312 pathway in yeast, forms gel-like condensates with Atg19 on the surface of Ape1
313 condensates to be sequestered by the isolation membrane (Yamasaki *et al*, 2020). This
314 association could also be mediated by partial wetting. These examples together with our
315 observations highlight the importance of LLPS and the wetting phenomena in various
316 selective autophagy processes.
317 LLPS may also be important for non-selective bulk autophagy. In yeast, the Atg1
318 complex (the ULK1 complex in mammals) forms pre-autophagosomal structures (PASs),
319 which have been shown to be condensates driven by LLPS (Fujioka *et al*, 2020). Phase
320 separation in this context provides a high local concentration of the Atg1 complex to
321 support the autoactivation of Atg1 kinase (Yamamoto *et al*, 2016). Mammalian autophagy
322 factors also accumulate at the autophagosome formation site; FIP200, a subunit of the
323 autophagy-initiation complex, undergoes LLPS triggered by calcium transients (Zheng *et al*,
324 2022). The liquid-like nature of these autophagy-initiating structures may also be important
325 for the recruitment of Atg9/ATG9 vesicles through the wetting effect.
326
327 **The importance of phase separation during mitophagy**
328 In contrast to Parkin-mediated mitophagy, hypoxia-induced mitophagy does not involve
329 autophagy adaptors, and instead, the outer mitochondrial membrane proteins NIX (also
330 known as BNIP3L) and BNIP3 directly interact with ATG8 homologs on the isolation
331 membrane (Novak *et al*, 2010; Onishi *et al*, 2021). In this context, ATG8 proteins interact
332 with NIX or BNIP3, likely in a one-to-one manner. This raises the problem of why phase
333 separation of autophagy adaptors is essential for Parkin-mediated mitophagy. One
334 possibility is that the quick induction and execution of Parkin-mediated mitophagy requires
335 amplification of the reactions through increased local concentration of adaptors and
336 autophagy-related proteins facilitated by LLPS. This is consistent with the fact that
337 mitophagy-inducing signals are also amplified by a mechanism involving phosphorylated
338 ubiquitin (Kane *et al*, 2014; Kazlauskaite *et al*, 2014; Koyano *et al*, 2014). Alternatively,

339 Parkin-mediated mitophagy requires a high level of precision and selectivity; mitophagy
340 should be induced only for damaged mitochondria, which is ensured by the recruitment and
341 retention of ATG9 vesicles only on phase-separated adaptor-positive mitochondria. This
342 strict specificity would enable proper quality control of the mitochondria. Further study
343 would be required to elucidate the functions and physiological importance of LLPS by
344 autophagy adaptors in mitophagy and beyond.
345

346 **Materials and Methods**

347

348 **Cell culture and generation of stable cell lines**

349 HeLa cells, HeLa penta-knockout (penta KO) cells, and human embryonic kidney (HEK)
350 293T cells authenticated by RIKEN were cultured in Dulbecco's modified Eagle's medium
351 (DMEM; D6546; Sigma-Aldrich) supplemented with 10% fetal bovine serum (FBS; 173012;
352 Sigma-Aldrich) and 2 mM L-glutamine (25030-081; Gibco) in a 5% CO_2 incubator at 37°C.
353 For stable expression, retrovirus was produced with HEK293T cells transfected with pMRX-
354 IP-based, pMRX-IB-based, pMRX-IU-based, or pMRX-IN-based retroviral plasmids, pCG-
355 VSV-G, and pCG-gag-pol by using Lipofectamine 2000 (11668019; Thermo Fisher
356 Scientific). After transfection, cells were further incubated at 37°C for 24h. The viral
357 supernatant was collected by filtration through a 0.45-μm filter unit (Ultrafree-MC; Millipore)
358 and then used for infection. Cells were plated onto 6-cm dishes 18 h before infection, and
359 the medium was replaced with viral supernatant diluted 1.5-fold with 8 μg/mL polybrene
360 (H9268; Sigma-Aldrich). Two days later, cells were selected in a medium containing 2
361 μg/mL puromycin (P8833; Sigma-Aldrich), 4 μg/mL blasticidin S hydrochloride (022-18713;
362 FUJIFILM Wako Pure Chemical Corporation), 1.5 mg/mL neomycin, or 250 μg/mL zeocin
363 (R25005; Thermo Fisher Scientific).

364

365 **Plasmids**

366 The pMRX-IPU, pMRX-IBU and pMRX-INU plasmids were generated by modifying the
367 multi-cloning site of pMRX-IP (Saitoh *et al*, 2002; Kitamura *et al*, 2003), pMRX-IB, and
368 pMRX-IN, respectively. DNA fragments encoding ubiquitin, p62 (NM_003900.5), OPTN
369 (NM_001008211.1), NBR1 (NM_001291571.2), NDP52 (NM_001261391.2), TAX1BP1
370 (NM_001206901.1), ATG9A (NM_001077198.3), LC3A (NM_032514.4), and LC3B
371 (NM_022818.5) were inserted into pMRX-IPU, pMRX-INU, or pMRX-IBU. DNAs encoding
372 the HA epitope, monomeric enhanced GFP with the A206K mutation (mGFP), codon-
373 optimized ultra-stable GFP (muGFP) (Scott *et al*, 2018), codon-optimized mRuby3 (Bajar *et*

374 *al*, 2016), HaloTag7 (G1891; Promega), 3×FLAG, and SNAP-tag (New England BioLabs,
375 N9181S) were used for tagging. The mitochondrial presequence of *Neurospora crassa* Fo-
376 ATPase subunit 9 (residues 1–69) was added to HaloTag7-SNAP to deliver the reporter into
377 the mitochondrial matrix (mtHalo-SNAP) (Eura, 2003). Truncated OPTN (OPTNΔUBAN, aa
378 445–502) was prepared by PCR-mediated site-directed mutagenesis. The resulting
379 plasmids were sequenced.
380
381 **Antibodies and reagents**
382 The primary antibodies used in this study were rabbit polyclonal anti-OPTN (Proteintech,
383 10837-AP), rabbit polyclonal anti-ATG9A (MBL, PD042), mouse monoclonal anti-Halo
384 (Promega, G9211), mouse monoclonal anti-HSP90 (BD Transduction Laboratories,
385 610419), and rabbit polyclonal anti-GFP (Thermo Fisher Scientific, A6455) antibodies. The
386 secondary antibodies used were HRP-conjugated goat polyclonal anti-rabbit IgG (Jackson
387 ImmunoResearch Laboratories, 111-035-144) and HRP-conjugated goat polyclonal anti-
388 mouse IgG (Jackson ImmunoResearch Laboratories, 115-035-003) antibodies. To induce
389 mitophagy, HeLa cells were treated with 10 μM carbonyl cyanide *m*-chlorophenyl hydrazine
390 (CCCP; Sigma-Aldrich) for 45 min, or 10 μM oligomycin (Cabiochem, 495455-10MGCN)
391 and 4 μM antimycin A (Sigma-Aldrich, A8674) for 18 h. After cells had been treated with
392 oligomycin and antimycin A for >6 h, 10 μM Q-VD-OPH (SM Biochemicals, SMPH001) was
393 added to block apoptotic cell death. To inhibit the formation of isolation membranes in the
394 1,6-hexanediol (Sigma-Aldrich, 240117-50G) treatment experiment, 20 μM wortmannin
395 (Sigma-Aldrich, W1628-1MG) was added into the medium.
396
397 **Immunoprecipitation and immunoblotting**
398 Cell lysates were prepared in a lysis buffer (50 mM Tris-HCl pH 7.4, 150 mM NaCl, 1 mM
399 EDTA, 1% Triton X-100, EDTA-free protease inhibitor cocktail [19543200; Roche]). After
400 centrifugation at 17,700 × *g* for 10 min, the supernatants were subjected to
401 immunoprecipitation using anti-FLAG M2 magnetic beads (M8823-1ML; Sigma-Aldrich).

402 Precipitated immunocomplexes were washed three times with lysis buffer and boiled in
403 sample buffer (46.7 mM Tris-HCl, pH 6.8, 5% glycerol, 1.67% sodium dodecyl sulfate,
404 1.55% dithiothreitol, and 0.02% bromophenol blue). For immunoprecipitation of ATG9
405 vesicles, cells were disrupted by Dounce homogenization with hypotonic lysis buffer (10
406 mM HEPES, pH 7.9, 1.5 mM $MgCl_2$ and 10 mM KCl, EDTA-free protease inhibitor cocktail
407 [19543200; Roche]). Disruption was carried out by applying 35 strokes while the cell
408 suspension was cooled on ice. The supernatants were subjected to immunoprecipitation
409 using anti-FLAG M2 magnetic beads (M8823-1ML; Sigma-Aldrich). For immunoblotting, the
410 samples were separated by SDS-PAGE and transferred to Immobilon-P polyvinylidene
411 difluoride membranes (Millipore, WBKLS0500) with the Trans-Blot Turbo Transfer System
412 (Bio-Rad). After incubation with the relevant antibody in 5% skim milk in 20 mM Tris-HCl,
413 150 mM NaCl, and 0.1% Tween 20 (02194841-CF; MP Biomedicals), the signals from
414 incubation with SuperSignal West Pico Chemiluminescent Substrate (Thermo Fisher
415 Scientific, 34579) were detected with the FUSION SOLO.7S.EDGE imaging system (Vilber-
416 Lourmat). Contrast and brightness adjustment and quantification were performed using the
417 image processing software Fiji (Schindelin *et al*, 2012).
418
419 **Fluorescence recovery after photobleaching**
420 In-cell fluorescence recovery after photobleaching (FRAP) analyses were performed with
421 an Olympus Fluoview FV3000 confocal microscope equipped with a 60× oil-immersion
422 objective lens (1.40 NA, Olympus). The chamber was maintained at 37°C and continuously
423 supplied with humidified 5% CO_2. Bleaching was performed using 80% laser power (488 or
424 561 nm laser), and images were captured every 5 s for 30 frames. Recovery curves and
425 fitting were analyzed using OriginPro 2022. Fluorescence intensity of the bleached spot, an
426 unbleached control spot, and the background was measured using the software package
427 Fiji. Background intensity was subtracted, and the intensity values of the region of interest
428 are reported relative to the pre-bleached images during image acquisition. Each data point
429 represents the mean and standard error of fluorescence intensities in more than three

430 unbleached (control) or bleached (experimental) spots.

431

432 **Live-cell imaging**

433 Living imaging was conducted with the Olympus SpinSR10 spinning-disk confocal super-
434 resolution microscope equipped with a Hamamatsu ORCA-Flash 4.0 camera, a UPLAPO
435 OHR 100 × (NA 1.50) lens, and the SORA disk in place. The microscope was operated with
436 Olympus cellSens Dimension 2.3 software. Cells were passaged onto a four-chamber
437 glass-bottom dish (Greiner Bio-One) more than 24 h before imaging. To induce mitophagy,
438 cells were incubated with 10 μM CCCP in the presence of 200 nM SF650-conjugated Halo
439 ligand (GoryoChemical, A308-02). Images were processed using the image processing
440 software package Fiji (Schindelin *et al*, 2012). Fluorescence intensity of indicated
441 fluorophores was measured by Fiji, and spline connected graphs were created using
442 OriginPro 2022 software.

443

444 **Immunofluorescence imaging**

445 Cells were fixed with 4% PFA in 0.1 M phosphate buffer (pH 7.3) for 15 min at room
446 temperature (RT) and washed with PBS. Fixed cells were incubated with 10 μg/mL digitonin
447 for 5 min at RT and washed with PBS. Then, cells were incubated with primary antibodies
448 diluted (1:1000) in blocking buffer (3% BSA, in PBS) for 1 h at RT, washed with PBS,
449 incubated with Alexa Fluor-conjugated secondary antibodies (1:1000) in blocking buffer for
450 60 min at RT, washed again, and mounted on coverslips. Colocalization was calculated by
451 Fiji plugins BIOP JACoP, with the threshold of the ATG9A channel fixed to 500. ATG9A-
452 positive areas out of GFP-positive areas were calculated to obtain the overlapping areas.

453

454 **Mathematical model of autophagy adaptor condensate formation**

455 We formulated a mathematical model of autophagy adaptor condensate formation. For the
456 case of two mitochondria approaching each other (Fig. 3A), the free energy, F, of the
457 system can be written as

$$F = \int (f_{int} + f_{ent}) dV\,, \tag{1}$$

with the interaction energy, f_{int}, and the entropic energy, f_{ent}, expressed as

$$f_{int} = \frac{\sigma}{2}(\nabla\phi_{ad})^2 - \chi_{self}\phi_{ad}^2 - \chi_{Ub}\phi_{Ub}\phi_{ad} + \chi_{Mt}\phi_{Mt}\phi_{ad}, \tag{2}$$

$$f_{ent} = \phi_{ad}\ln\phi_{ad} + \phi_{sol}\ln\phi_{sol}\,, \tag{3}$$

where ϕ_{ad}, ϕ_{Ub}, and $\phi_{sol} = 1 - \phi_{ad} - \phi_{Ub} - \phi_{Mt}$ are the adaptor, ubiquitin, and solvent concentrations, respectively, χ_{self} and χ_{Ub} represent the strength of the adaptor self-interaction and adaptor–ubiquitin interaction, respectively, σ represents the surface tension of the condensates, and χ_{Mt} represents the mitochondrial area exclusion effect, introduced to prevent proteins from entering the mitochondrial interior (ϕ_{Mt}).

For the case in which an isolation membrane surrounded a mitochondrion (Fig. 3C), the interaction energy, f_{int}, is instead expressed as

$$f_{int} = \frac{\sigma}{2}(\nabla\phi_{ad})^2 - \chi_{self}\phi_{ad}^2 - \chi_{Ub}\phi_{Ub}\phi_{ad} - \chi_{LC3}\phi_{LC3}\phi_{ad} + \chi_{Mt}\phi_{Mt}\phi_{ad} + \chi_{IM}\phi_{IM}\phi_{ad}, \tag{5}$$

where ϕ_{LC3} and χ_{LC3} represent the LC3 concentrations and the strength of the adaptor–LC3 interaction, respectively, and χ_{IM} represents the mitochondrial area exclusion effect, introduced to prevent proteins from entering the lumen of the isolation membrane (ϕ_{IM}). The solvent concentration that appears in the entropic energy (3) was also modified to $\phi_{sol} = 1 - \phi_{ad} - \phi_{Ub} - \phi_{LC3} - \phi_{Mt} - \phi_{IM}$.

For the numerical simulation, the space was discretized by a lattice with 10 nm on each side, and a concentration field was assigned to each location. The time evolution of the system was assumed to follow the Cahn–Hilliard equation,

$$\frac{\partial\phi_{ad}}{\partial t} = \frac{\partial}{\partial\vec{x}}\left[M\frac{\partial}{\partial\vec{x}}\left(\frac{\delta F}{\delta\phi_{ad}}\right)\right], \tag{4}$$

which is commonly used in analyses of phase separation dynamics (Berry *et al*, 2018). Here, $M = D/k_BT$ is the mobility of the protein with the diffusion constant $D = 10$ μm²/sec (Milo & Phillips, 2015) expressed in terms of the Boltzmann constant k_B and temperature T. We considered a 3000 nm × 3000 nm square region with periodic boundary conditions containing two mitochondria and surrounding cytosolic components as a system and assumed that adaptor proteins are uniformly distributed in the cytosol around mitochondria

at a concentration of $\phi = 0.1$ in the initial state.

Statistical analysis

Statistical analysis was performed using OriginPro 2022 software. The statistical methods used for each analysis are specified in the figure legends.

Acknowledgments

We thank Michael Lazarou (Walter and Eliza Hall Institute of Medical Research) for providing pentaKO HeLa cells, Toshio Kitamura for pMXs-IP (The University of Tokyo), Shoji Yamaoka (Tokyo Medical and Dental University, Tokyo, Japan) for pMRXIP, and Teruhito Yasui (National Institutes of Biomedical Innovation, Health and Nutrition (NIBIOHN), Osaka, Japan) for pCG-VSV-G and pCG-gag-pol. pKanCMV-mClover3-mRuby3 was a gift from Michael Lin (Addgene plasmid # 74252 ; http://n2t.net/addgene:74252 ; RRID:Addgene_74252).

This work was supported by the Exploratory Research for Advanced Technology (ERATO) research funding program of the Japan Science and Technology Agency (JST) (JPMJER1702 to NM), a Grant-in-Aid for Specially Promoted Research (22H04919 to NM) and a Grant-in-Aid for Scientific Research (C) (23K05715 to Y.S.) from the Japan Society for the Promotion of Science (JSPS), and German Research Foundation (Project 460056461 to RLK). The numerical computations have been performed with the RIKEN supercomputer system (HOKUSAI).

Author contributions

Z.Y., S.Y., H.C. R.L.K., and N.M. designed the project. Z.Y. performed most of the cell biology experiments. Y.S. developed the mathematical model. Z.Y., S.Y., Y.S., R.L.K., and N.M. wrote the manuscript. All authors analyzed and discussed the results and commented on the manuscript.

Disclosure and competing interests statement

The authors declare that they have no conflict of interest.

References

Agudo-Canalejo J, Schultz SW, Chino H, Migliano SM, Saito C, Koyama-Honda I, Stenmark H, Brech A, May AI, Mizushima N, *et al* (2021) Wetting regulates autophagy of phase-separated compartments and the cytosol. *Nature* 591: 142–146

Bajar BT, Wang ES, Lam AJ, Kim BB, Jacobs CL, Howe ES, Davidson MW, Lin MZ & Chu J (2016) Improving brightness and photostability of green and red fluorescent proteins for live cell imaging and FRET reporting. *Sci Rep* 6: 20889

Berry J, Brangwynne CP & Haataja M (2018) Physical principles of intracellular organization via active and passive phase transitions. *Reports on Progress in Physics* 81: 046601

Eura Y (2003) Two Mitofusin Proteins, Mammalian Homologues of FZO, with Distinct Functions Are Both Required for Mitochondrial Fusion. *J Biochem* 134: 333–344

Fujioka Y, Alam JM, Noshiro D, Mouri K, Ando T, Okada Y, May AI, Knorr RL, Suzuki K, Ohsumi Y, *et al* (2020) Phase separation organizes the site of autophagosome formation. *Nature* 578: 301–305

Gallagher ER & Holzbaur ELF (2023) The selective autophagy adaptor p62/SQSTM1 forms phase condensates regulated by HSP27 that facilitate the clearance of damaged lysosomes via lysophagy. *Cell Rep* 42: 112037

Ganley IG & Simonsen A (2022) Diversity of mitophagy pathways at a glance. *J Cell Sci* 135: jcs259748

Geisler S, Holmström KM, Skujat D, Fiesel FC, Rothfuss OC, Kahle PJ & Springer W (2010) PINK1/Parkin-mediated mitophagy is dependent on VDAC1 and p62/SQSTM1. *Nat Cell Biol* 12: 119–131

Gouveia B, Kim Y, Shaevitz JW, Petry S, Stone HA & Brangwynne CP (2022) Capillary forces generated by biomolecular condensates. *Nature* 609: 255–264

Gubas A & Dikic I (2022) A guide to the regulation of selective autophagy receptors. *FEBS J* 289: 75–89

Heo J-M, Ordureau A, Paulo JA, Rinehart J & Harper JW (2015) The PINK1-PARKIN Mitochondrial Ubiquitylation Pathway Drives a Program of OPTN/NDP52 Recruitment and TBK1 Activation to Promote Mitophagy. *Mol Cell* 60: 7–20

Hirose T, Ninomiya K, Nakagawa S & Yamazaki T (2023) A guide to membraneless organelles and their various roles in gene regulation. *Nat Rev Mol Cell Biol* 24: 288–304

Hyman AA, Weber CA & Jülicher F (2014) Liquid-Liquid Phase Separation in Biology. *Annu Rev Cell Dev Biol* 30: 39–58

Itakura E, Kishi-Itakura C, Koyama-Honda I & Mizushima N (2012) Structures containing Atg9A and the ULK1 complex independently target depolarized mitochondria at initial stages of Parkin-mediated mitophagy. *J Cell Sci* 125: 1488–1499

Kane LA, Lazarou M, Fogel AI, Li Y, Yamano K, Sarraf SA, Banerjee S & Youle RJ (2014) PINK1 phosphorylates ubiquitin to activate Parkin E3 ubiquitin ligase activity. *Journal of Cell Biology* 205: 143–153

Kazlauskaite A, Kondapalli C, Gourlay R, Campbell DG, Ritorto MS, Hofmann K, Alessi DR,

557 Knebel A, Trost M & Muqit MMK (2014) Parkin is activated by PINK1-dependent
558 phosphorylation of ubiquitin at Ser65. *Biochemical Journal* 460: 127–141
559 Kitamura T, Koshino Y, Shibata F, Oki T, Nakajima H, Nosaka T & Kumagai H (2003)
560 Retrovirus-mediated gene transfer and expression cloning: powerful tools in functional
561 genomics. *Exp Hematol* 31: 1007–1014
562 Koyano F, Okatsu K, Kosako H, Tamura Y, Go E, Kimura M, Kimura Y, Tsuchiya H, Yoshihara
563 H, Hirokawa T, *et al* (2014) Ubiquitin is phosphorylated by PINK1 to activate parkin.
564 *Nature* 510: 162–166
565 Kusumaatmaja H, May AI, Feeney M, McKenna JF, Mizushima N, Frigerio L & Knorr RL
566 (2021a) Wetting of phase-separated droplets on plant vacuole membranes leads to a
567 competition between tonoplast budding and nanotube formation. *Proceedings of the*
568 *National Academy of Sciences* 118: e2024109118
569 Kusumaatmaja H, May AI & Knorr RL (2021b) Intracellular wetting mediates contacts
570 between liquid compartments and membrane-bound organelles. *J Cell Biol* 220:
571 e202103175
572 Lamark T & Johansen T (2021) Mechanisms of Selective Autophagy. *Annu Rev Cell Dev Biol*
573 37: 143–169
574 Lazarou M, Sliter DA, Kane LA, Sarraf SA, Wang C, Burman JL, Sideris DP, Fogel AI & Youle
575 RJ (2015) The ubiquitin kinase PINK1 recruits autophagy receptors to induce mitophagy.
576 *Nature* 524: 309–314
577 Ma X, Li P & Ge L (2023) Targeting of biomolecular condensates to the autophagy pathway.
578 *Trends Cell Biol* 33: 505–516
579 McSwiggen DT, Mir M, Darzacq X & Tjian R (2019) Evaluating phase separation in live cells:
580 diagnosis, caveats, and functional consequences. *Genes Dev* 33: 1619–1634
581 Milo R & Phillips R (2015) Cell Biology by the Numbers Garland Science
582 Milovanovic D & De Camilli P (2017) Synaptic Vesicle Clusters at Synapses: A Distinct Liquid
583 Phase? *Neuron* 93: 995–1002
584 Mizushima N & Levine B (2020) Autophagy in Human Diseases. *New England Journal of*
585 *Medicine* 383: 1564–1576
586 Moore AS & Holzbaur ELF (2016) Dynamic recruitment and activation of ALS-associated
587 TBK1 with its target optineurin are required for efficient mitophagy. *Proceedings of the*
588 *National Academy of Sciences* 113: E3349–E3358
589 Musacchio A (2022) On the role of phase separation in the biogenesis of membraneless
590 compartments. *EMBO J* 41: e109952
591 Nakatogawa H (2020) Mechanisms governing autophagosome biogenesis. *Nat Rev Mol Cell*
592 *Biol* 21: 439–458
593 Noda NN, Wang Z & Zhang H (2020) Liquid–liquid phase separation in autophagy. *Journal*
594 *of Cell Biology* 219: e202004062
595 Novak I, Kirkin V, McEwan DG, Zhang J, Wild P, Rozenknop A, Rogov V, Löhr F, Popovic D,
596 Occhipinti A, *et al* (2010) Nix is a selective autophagy receptor for mitochondrial
597 clearance. *EMBO Rep* 11: 45–51
598 O'Loughlin T, Kruppa AJ, Ribeiro ALR, Edgar JR, Ghannam A, Smith AM & Buss F (2020)

599 OPTN recruitment to a Golgi-proximal compartment regulates immune signalling and
600 cytokine secretion. *J Cell Sci* 133: 1–15
601 Onishi M, Yamano K, Sato M, Matsuda N & Okamoto K (2021) Molecular mechanisms and
602 physiological functions of mitophagy. *EMBO J* 40: e104705
603 Park D, Wu Y, Wang X, Gowrishankar S, Baublis A & De Camilli P (2023) Synaptic vesicle
604 proteins and ATG9A self-organize in distinct vesicle phases within synapsin
605 condensates. *Nat Commun* 14: 455
606 Peng S, Chen X-H, Chen S, Zhang J, Wang C, Liu W, Zhang D, Su Y & Zhang X (2021)
607 Phase separation of Nur77 mediates celastrol-induced mitophagy by promoting the
608 liquidity of p62/SQSTM1 condensates. *Nat Commun* 12: 5989
609 Rothbauer U, Zolghadr K, Muyldermans S, Schepers A, Cardoso MC & Leonhardt H (2008)
610 A Versatile Nanotrap for Biochemical and Functional Studies with Fluorescent Fusion
611 Proteins. *Molecular & Cellular Proteomics* 7: 282–289
612 Saitoh T, Nakano H, Yamamoto N & Yamaoka S (2002) Lymphotoxin-beta receptor mediates
613 NEMO-independent NF-kappaB activation. *FEBS Lett* 532: 45–51
614 Sansevrino R, Hoffmann C & Milovanovic D (2023) Condensate biology of synaptic vesicle
615 clusters. *Trends Neurosci* 46: 293–306
616 Schindelin J, Arganda-Carreras I, Frise E, Kaynig V, Longair M, Pietzsch T, Preibisch S,
617 Rueden C, Saalfeld S, Schmid B, *et al* (2012) Fiji: an open-source platform for
618 biological-image analysis. *Nat Methods* 9: 676–682
619 Scott DJ, Gunn NJ, Yong KJ, Wimmer VC, Veldhuis NA, Challis LM, Haidar M, Petrou S,
620 Bathgate RAD & Griffin MDW (2018) A Novel Ultra-Stable, Monomeric Green
621 Fluorescent Protein For Direct Volumetric Imaging of Whole Organs Using CLARITY.
622 *Sci Rep* 8: 667
623 Style RW, Jagota A, Hui C-Y & Dufresne ER (2017) Elastocapillarity: Surface Tension and
624 the Mechanics of Soft Solids. *Annu Rev Condens Matter Phys* 8: 99–118
625 Sun D, Wu R, Zheng J, Li P & Yu L (2018) Polyubiquitin chain-induced p62 phase separation
626 drives autophagic cargo segregation. *Cell Res* 28: 405–415
627 Taylor NO, Wei M-T, Stone HA & Brangwynne CP (2019) Quantifying Dynamics in Phase-
628 Separated Condensates Using Fluorescence Recovery after Photobleaching. *Biophys*
629 *J* 117: 1285–1300
630 Turco E, Savova A, Gere F, Ferrari L, Romanov J, Schuschnig M & Martens S (2021)
631 Reconstitution defines the roles of p62, NBR1 and TAX1BP1 in ubiquitin condensate
632 formation and autophagy initiation. *Nat Commun* 12: 5212
633 Vargas JNS, Hamasaki M, Kawabata T, Youle RJ & Yoshimori T (2023) The mechanisms and
634 roles of selective autophagy in mammals. *Nat Rev Mol Cell Biol* 24: 167–185
635 Wexler JS, Heard TM & Stone HA (2014) Capillary Bridges between Soft Substrates. *Phys*
636 *Rev Lett* 112: 066102
637 Wong YC & Holzbaur ELF (2014) Optineurin is an autophagy receptor for damaged
638 mitochondria in parkin-mediated mitophagy that is disrupted by an ALS-linked mutation.
639 *Proceedings of the National Academy of Sciences* 111: E4439–E4448
640 Yamamoto H, Fujioka Y, Suzuki SW, Noshiro D, Suzuki H, Kondo-Kakuta C, Kimura Y, Hirano

641 H, Ando T, Noda NN, *et al* (2016) The Intrinsically Disordered Protein Atg13 Mediates
642 Supramolecular Assembly of Autophagy Initiation Complexes. *Dev Cell* 38: 86–99
643 Yamamoto H, Kakuta S, Watanabe TM, Kitamura A, Sekito T, Kondo-Kakuta C, Ichikawa R,
644 Kinjo M & Ohsumi Y (2012) Atg9 vesicles are an important membrane source during
645 early steps of autophagosome formation. *Journal of Cell Biology* 198: 219–233
646 Yamano K, Kikuchi R, Kojima W, Hayashida R, Koyano F, Kawawaki J, Shoda T, Demizu Y,
647 Naito M, Tanaka K, *et al* (2020) Critical role of mitochondrial ubiquitination and the
648 OPTN-ATG9A axis in mitophagy. *J Cell Biol* 219: e201912144
649 Yamasaki A, Alam JM, Noshiro D, Hirata E, Fujioka Y, Suzuki K, Ohsumi Y & Noda NN (2020)
650 Liquidity Is a Critical Determinant for Selective Autophagy of Protein Condensates. *Mol*
651 *Cell* 77: 1163-1175.e9
652 Yim WW-Y, Yamamoto H & Mizushima N (2022) A pulse-chasable reporter processing assay
653 for mammalian autophagic flux with HaloTag. *Elife* 11: e78923
654 Zaffagnini G, Savova A, Danieli A, Romanov J, Tremel S, Ebner M, Peterbauer T, Sztacho M,
655 Trapannone R, Tarafder AK, *et al* (2018) p62 filaments capture and present
656 ubiquitinated cargos for autophagy. *EMBO J* 37: e98308
657 Zheng Q, Chen Y, Chen D, Zhao H, Feng Y, Meng Q, Zhao Y & Zhang H (2022) Calcium
658 transients on the ER surface trigger liquid-liquid phase separation of FIP200 to specify
659 autophagosome initiation sites. *Cell* 185: 4082-4098.e22

660

661

662 **Figure legends**

663

664 **Figure 1. Autophagy adaptors show distinct distributions during Parkin-mediated**
665 **mitophagy.**

666 (A, B, and E) Representative images (left) and spline graphs of the intensity profiles along
667 the indicated lines in the respective images (right) of wild-type HeLa cells (A and B) or
668 HeLa cells lacking all five autophagy adaptors (penta KO cells) (E) expressing one of the
669 GFP-tagged autophagy adaptors or ubiquitin, mRuby–Omp25, and HaloTag7–LC3B at 45
670 min after 20 μM CCCP treatment. Separate mitochondria without contacting other
671 mitochondria or isolation membranes (A; Mt) or mitochondria with an isolation membrane
672 (B and E; Mt–IM) are shown. The *y*-axis in each of the graphs indicates the fluorescence
673 intensity. Scale bars indicate 1 μm.

674 (C and F) The relative intensity of GFP-tagged adaptors or ubiquitin (a and b) in LC3B-
675 positive areas compared with LC3B-negative areas in panels B and E. GFP signals were
676 normalized to the mRuby–Omp25 signals (a′ and b′) using the formula Relative Intensity =
677 (a/b)/(a′/b′), where a and a′ represent the intensities in the LC3B-positive area, and b and b′
678 represent the intensities in the LC3B-negative area. Solid horizontal bars indicate the
679 means, and dots indicate the data from five structures. Differences were statistically
680 analyzed by one-way analysis of variance with Dunnett's post-hoc test.

681 (D) Immunostaining of endogenous OPTN or NDP52 in wild-type HeLa cells expressing
682 mRuby–Omp25 and HaloTag7–LC3B at 45 min after 20 μM CCCP treatment. Scale bars
683 indicate 4 μm and 1 μm (magnified images).

684

685 **Figure 2. OPTN and NDP52 show a dynamic exchange between the mitochondrial**
686 **surface and cytosol.**

687 (A–D) Representative images (A and C) and quantification (B and D) of GFP fluorescence
688 recovery after photobleaching (FRAP) on separate mitochondria (Mt) (A and B) or on
689 mitochondria with an isolation membrane (Mt–IM) (C and D) in HeLa cells lacking all five

690 autophagy adaptors (penta KO cells) expressing GFP-tagged adaptors or ubiquitin at 45
691 min after 20 μM CCCP treatment. The photobleached areas are indicated by dotted lines.
692 The magnified panels display time-lapse images of the photobleached areas. Scale bars
693 indicate 2 μm and 1 μm (magnified images). Data were collected from four structures and
694 were fitted to the equation $y = a*(1 - \exp(-b*x))$. The dark shaded areas represent the 95%
695 confidence intervals, and the light shaded areas represent the 95% prediction intervals.
696 (E) Penta KO cells expressing GFP–OPTN at 45 min after 20 μM CCCP and 20 μM
697 wortmannin treatment. Wortmannin was added to inhibit autophagosome formation so that
698 OPTN would not be sequestered in a closed compartment. Images of cells before (upper
699 panels) and 2 min after (lower panels) the addition of 10% 1,6-hexanediol are displayed.
700 Scale bars indicate 5 μm and 2 μm (magnified images).
701
702 **Figure 3. Mathematical models of condensate formation and localization of**
703 **autophagy adaptors.**
704 (A) Schematic diagram of two separated mitochondria.
705 (B) Sheet-like condensates of autophagy adaptors on mitochondria deform when the inter-
706 mitochondrial distance d_{Mt} was changed. The strength of adaptor self-interaction (χ_{self}),
707 adaptor–ubiquitin interaction (χ_{Ub}), mitochondrial area exclusion (χ_{Mt}) and surface tension
708 (σ) were set to $\chi_{self} = 3k_BT$, $\chi_{Ub} = 12k_BT$, $\chi_{Mt} = 5k_BT$, and $\sigma = k_BT$, respectively. The
709 color indicates the adaptor concentration (ϕ_{ad}). Arrowheads indicate autophagy adaptors
710 filling the cleft between the two mitochondria.
711 (C) Schematic diagram of a single mitochondrion with an isolation membrane.
712 (D) Sheet-like condensates of autophagy adaptors on mitochondria deformed when the
713 isolation membrane (arrowheads) appeared and the angle α surrounding the mitochondria
714 changed. The strength of adaptor self-interaction (χ_{self}), adaptor–ubiquitin interaction (χ_{Ub}),
715 adaptor–LC3 interaction (χ_{LC3}), mitochondrial area exclusion (χ_{Mt}), isolation membrane
716 area exclusion (χ_{IM}), and surface tension (σ) were set to $\chi_{self} = 3k_BT$, $\chi_{Ub} = \chi_{LC3} = 12k_BT$,
717 $\chi_{Mt} = \chi_{IM} = 5k_BT$, and $\sigma = k_BT$, respectively. The color indicates the adaptor concentration

718 (ϕ_{ad}).

719

720 **Figure 4. OPTN condensates redistribute upon contact with membranes.**

721 (A–D) Time-lapse images (A and C) and spline graphs (B and D) of two separate
722 mitochondria approaching and contacting each other. Events of the attachment of two
723 mitochondria with comparable sizes (A and B) and with differing sizes (C and D) were
724 observed. The line graphs represent the intensity profiles along the indicated lines in the
725 respective images shown (B and D). The arrowheads indicate redistributed OPTN signals
726 filling the cleft between two adjacent mitochondria. Scale bars indicate 1 μm. See also
727 Movie EV1 for the time-lapse video corresponding to (C).

728 (E and F) Time-lapse images (E) and a spline graph (F) of a mitochondrion with an isolation
729 membrane elongating on its surface. The arrowhead indicates the elongating isolation
730 membrane. The line graph represent the intensity profiles along the indicated lines in the
731 respective images shown. Scale bars indicate 1 μm. See also Movie EV2 for the time-lapse
732 video corresponding to (E).

733

734 **Figure 5. Liquid-like property of OPTN condensates is required for mitophagy.**

735 (A) HeLa cells lacking all five autophagy adaptors (penta KO cells) expressing both GPF–
736 OPTN and mRuby–Ub (top), both GFP–OPTNΔUBAN and mRuby–Ub (middle), or both
737 GFP–OPTNΔUBAN and anti-GFP nanobody–mRuby–Ub (bottom) at 45 min after 20 μM
738 CCCP treatment. Time-lapse images of GFP FRAP are shown. Photobleached areas are
739 circled by dotted lines. Scale bars indicate 4 μm and 2 μm (magnified images).

740 (B) Interaction between GFP–OPTN mutants and FLAG–Ub or FLAG–nanobody–Ub was
741 investigated by immunoprecipitation with an anti-FLAG antibody and immunoblotting with
742 an anti-GFP antibody.

743 (C) Quantification of GFP FRAP on separate mitochondria (Mt) in penta KO cells
744 expressing both GFP–OPTN and mRuby–Ub or both GFP–OPTNΔUBAN and anti-GFP
745 nanobody–mRuby–Ub at 45 min after 20 μM CCCP treatment. Data were collected from

746 four structures and were fitted to the equation $y = a*(1 - \exp(-b*x))$. The dark shading
747 represent the 95% confidence intervals, and the light shading represent the 95% prediction
748 intervals.
749 (D and E) Representative data (D) and quantification (E) of HaloTag (Halo) processing
750 assay using cells expressing the indicated OPTN and Ub constructs. Cells expressing the
751 mtHalo–SNAP mitophagy reporter were treated without (0 h) and with 1 μM oligomycin and
752 2 μM antimycin for 18 h. The amount of processed Halo (proc. Halo) indicates the relative
753 amount of mitochondria degraded by the lysosomes. Solid horizontal bars indicate the
754 means, and dots indicate the data from four independent experiments. Differences were
755 statistically analyzed by one-way analysis of variance with Dunnett's post-hoc test.
756
757 **Figure 6. Liquid-like property of OPTN condensates is required for the recruitment of**
758 **ATG9 vesicles.**
759 (A and B) Localization of ATG9 vesicles under normal (CCCP−) or mitophagy-inducing
760 conditions (CCCP+, 60 min) (A) and quantification (B) of ATG9A colocalization with
761 mitochondria. Endogenous ATG9 was immunostained in penta KO cells expressing both
762 GFP–OPTN and mRuby–Ub or both GFP–OPTNΔUBAN and mRuby–nanobody–Ub
763 together with mitochondrially targeted Halo–SNAP (mtHalo–SNAP). Scale bars indicate 4
764 μm and 2 μm (magnified images). Solid horizontal bars indicate the means, each dot
765 indicates the mean value from one field of view with ≥10 cells (n=15). Differences were
766 statistically analyzed by one-way analysis of variance with Dunnett's post-hoc test.
767 (C and D) Representative data (C) and quantification (D) of organelle immunoprecipitation
768 in cells expressing GFP–OPTN or GFP–OPTNΔUBAN in the presence or absence of
769 FLAG-ATG9A. ATG9 vesicles were immunoprecipitated by FLAG M2 beads and GFP was
770 blotted to detect the interaction between GFP–OPTN (WT or ΔUBAN) and ATG9 vesicles at
771 60 min after 20 μM CCCP treatment. Solid horizontal bars indicate the means, and dots
772 indicate the data from five independent experiments. Differences were statistically analyzed
773 by one-way analysis of variance with Dunnett's post-hoc test.

774 (E) The models of ATG9 vesicle recruitment (left) and isolation membrane elongation (right)
775 mediated by liquid-like OPTN condensates. Partial or complete wetting of phase-separated
776 OPTN enables the recruitment of ATG9 vesicles to ubiquitinated mitochondria (left). Wetting
777 of OPTN on mitochondria and isolation membranes also facilitates the engulfment of
778 mitochondria by the isolation membranes (right).
779
780 **Figure EV1. Localization of autophagy adaptors between mitochondria during**
781 **Parkin-mediated mitophagy.**
782 (A and C) Representative images (left) and spline graphs of the intensity profiles along the
783 indicated lines (right) of wild-type HeLa cells (A) or HeLa cells lacking all five autophagy
784 adaptors (penta KO cells) (C) expressing one of the GFP–tagged autophagy adaptors or
785 ubiquitin and mRuby–Omp25 at 45 min after 20 μM CCCP treatment. Mitochondrial
786 clusters (Mt–Mt) are shown. The *y*-axis in each of the graphs indicates the fluorescence
787 intensity.
788 (B and D) The relative intensity of each adaptor was calculated as in Figure 1C. Solid
789 horizontal bars indicate the means, and dots indicate the data from five structures.
790 Differences were statistically analyzed by one-way ANOVA with Dunnett's post-hoc test.
791
792 **Movie EV1. OPTN condensates redistribute upon mitochondrial contact.**
793 Time-lapse video of two separate mitochondria approaching and contacting each other (30s
794 per frame). Scale bars indicate 1 μm. See also Figure 4C and D.
795
796 **Movie EV2. OPTN condensates redistribute upon mitochondria–isolation membrane**
797 **contact.**
798 Time-lapse video of a mitochondrion with an isolation membrane elongating on its surface
799 (30s per frame). Scale bars indicate 1 μm. See also Figure 4E and F.

Figure 1

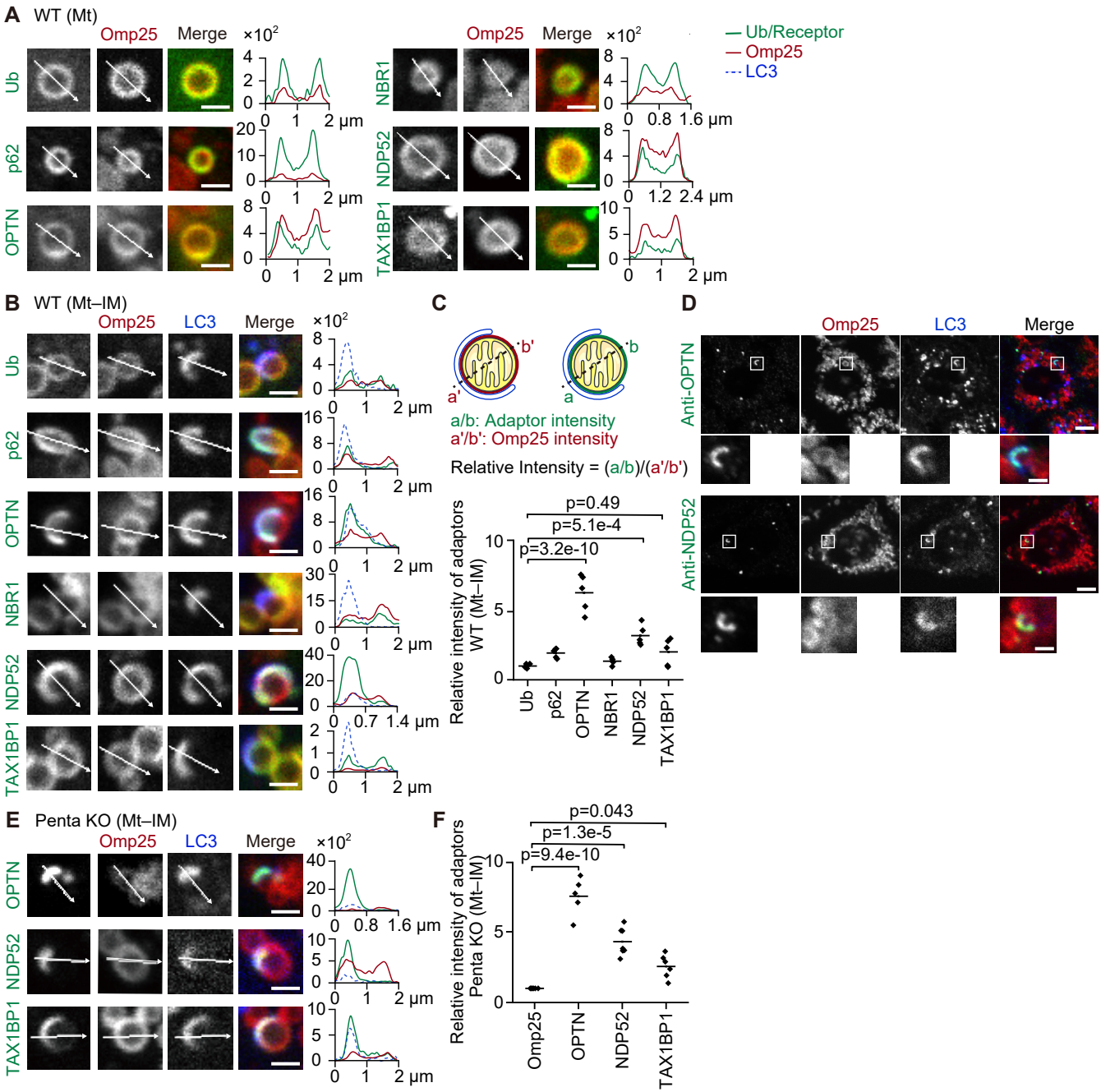

Figure 1. Autophagy adaptors show distinct distributions during Parkin-mediated mitophagy.
(A, B, and E) Representative images (left) and spline graphs of the intensity profiles along the indicated lines in the respective images (right) of wild-type HeLa cells (A and B) or penta KO cells (E) expressing one of the GFP-tagged autophagy adaptors or ubiquitin, mRuby–Omp25 and HaloTag7–LC3B at 45 min after 20 μM CCCP treatment. Single mitochondria without contacting other mitochondria or isolation membranes (A; Mt) or mitochondria with an isolation membrane (B and E; Mt–IM) are shown. The Y axis in the graphs indicates the fluorescence intensity. Scale bars, 1 μm.
(C and F) The relative intensity of GFP-tagged adaptors or ubiquitin (a and b) in LC3B-positive areas compared to LC3B-negative areas in panels B and E. GFP signals were normalized to the mRuby–Omp25 signals (a' and b') using the indicated formula: Relative Intensity = (a/b)/(a' /b'), where a and a' represent the intensities in the LC3B-positive area, and b and b' represent the intensities in the LC3B-negative area. Solid bars indicate the means and dots indicate the data from 5 structures. Differences were statistically analyzed by one-way ANOVA with Dunnett' s post hoc test.
(D) Immunostaining of endogenous OPTN or NDP52 in wild-type HeLa cells expressing mRuby–Omp25 and HaloTag7–LC3B at 45 min after 20 uM CCCP treatment. Scale bars, 4 um and 1 um (magnified images).

Figure 2

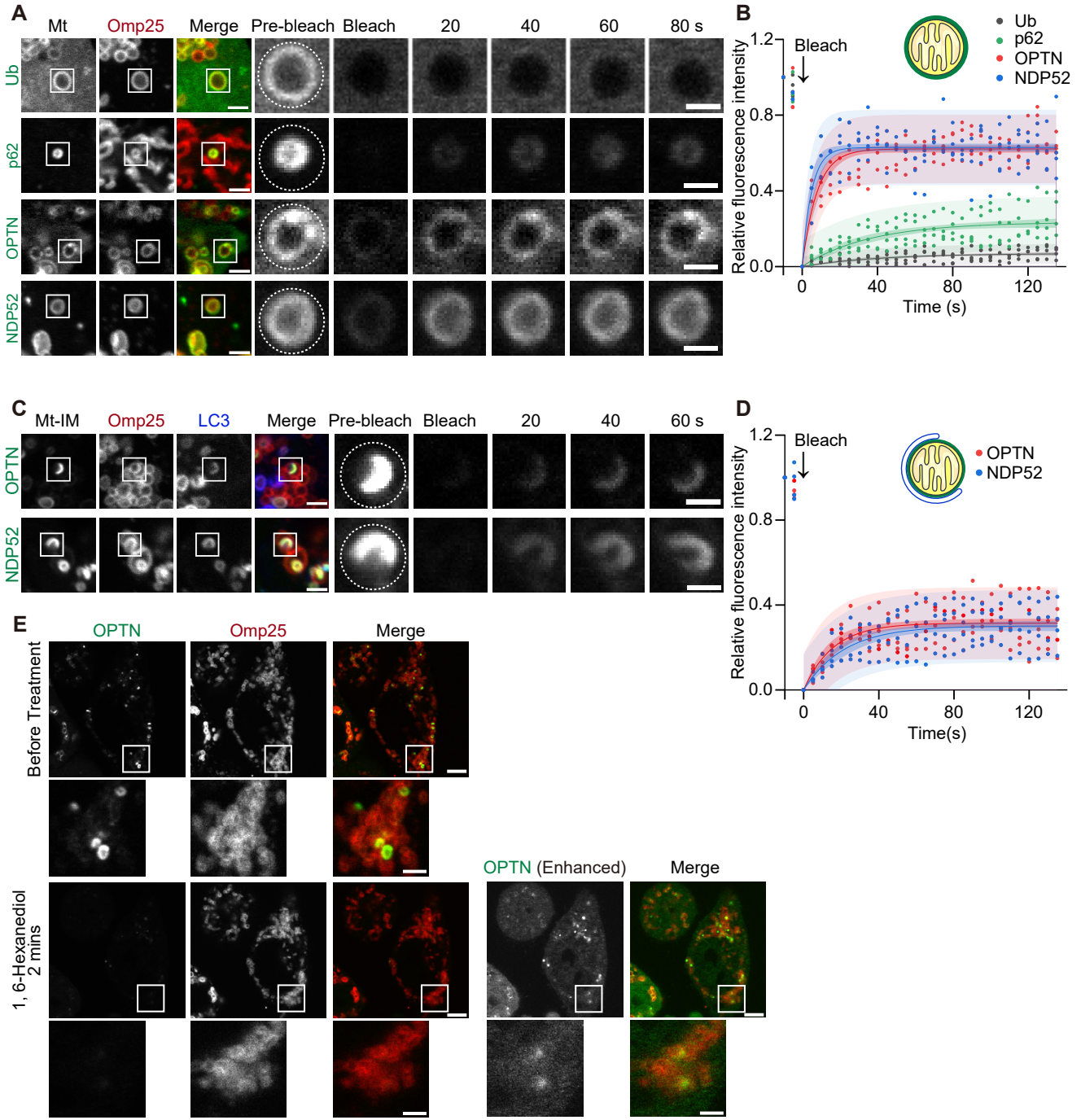

Figure 2. OPTN and NDP52 show a dynamic exchange between the mitochondrial surface and cytosol.
(A–D) Representative images (A and C) and quantification (B and D) of GFP FRAP on single mitochondria (Mt) (A and B) or on mitochondria with an isolation membrane (Mt–IM) (C and D) in penta KO cells expressing GFP-tagged adaptors or ubiquitin at 45 min after 20 μM CCCP treatment. The photobleached areas are indicated by dotted lines. The magnified panels display time-lapse images of the photobleached areas. Scale bars, 2 μm and 1 μm (magnified images). Data were collected from 4 structures and were fitted to the equation y = a*(1 - exp(-b*x)). The dark shadows represent the 95% confidence intervals, and the light shadows represent the 95% prediction intervals.
(E) Penta KO cells expressing GFP–OPTN at 45 min after 20 μM CCCP and 20 μM wortmannin treatment. Wortmannin was added to inhibit autophagosome formation so that OPTN is not sequestered in a closed compartment. Images of cells before (upper panels) and 2 min after (lower panels) the addition of 10% 1,6-hexanediol are displayed. Scale bars, 5 μm and 2 μm (magnified images).

Figure 3

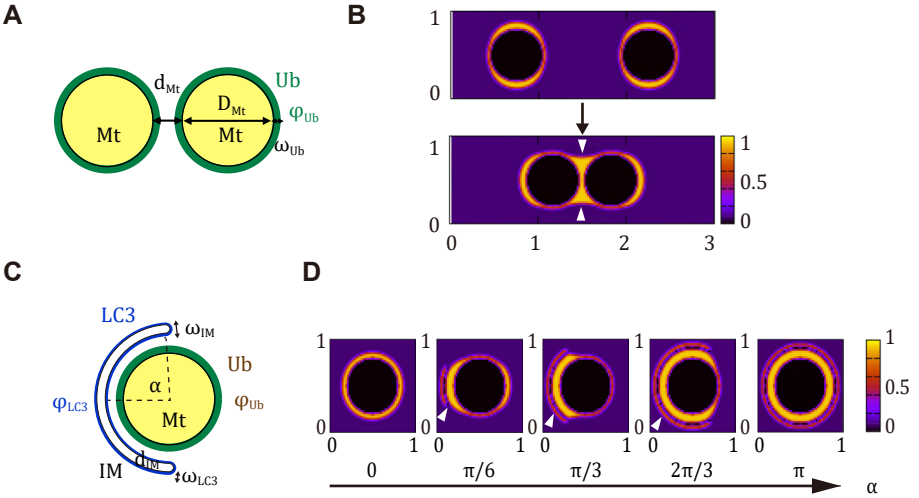

Figure 3. Mathematical models of condensate formation and localization of autophagy adaptors.
(A) Schematic diagram of two separated mitochondria.
(B) Sheet-like condensates of autophagy adaptors on mitochondria deform when the inter-mitochondrial distance d_{Mt} was changed. The strength of adaptor self-interaction (χ_{self}), adaptor-ubiquitin interaction (χ_{Ub}), mitochondrial area exclusion (χ_{Mt}) and surface tension (σ) were set to $\chi_{self}=3k_BT$, $\chi_{Ub}=12k_BT$, $\chi_{Mt}=5k_BT$, and $\sigma=k_BT$ respectively. The color indicated the adaptor concentration (ϕ_{ad}). Arrowheads indicate autophagy adaptors filling the cleft between the two mitochondria.
(C) Schematic diagram of a mitochondrion with an isolation membrane.
(D) Sheet-like condensates of autophagy adaptors on mitochondria deformed when the isolation membrane (arrowheads) appeared and the angle α surrounding the mitochondria changed. The strength of adaptor self-interaction (χ_{self}), adaptor-ubiquitin interaction (χ_{Ub}), adaptor-LC3 interaction (χ_{LC3}), mitochondrial area exclusion (χ_{Mt}), isolation membrane area exclusion (χ_{IM}), and surface tension (σ) were set to $\chi_{Ub}=\chi_{LC3}=12k_BT$ and $\chi_{self}=3k_BT$. $\sigma=k_BT$ and $\chi_{Mt}=\chi_{IM}=5k_BT$. The color indicated the adaptor concentration (ϕ_{ad}).

Figure 4

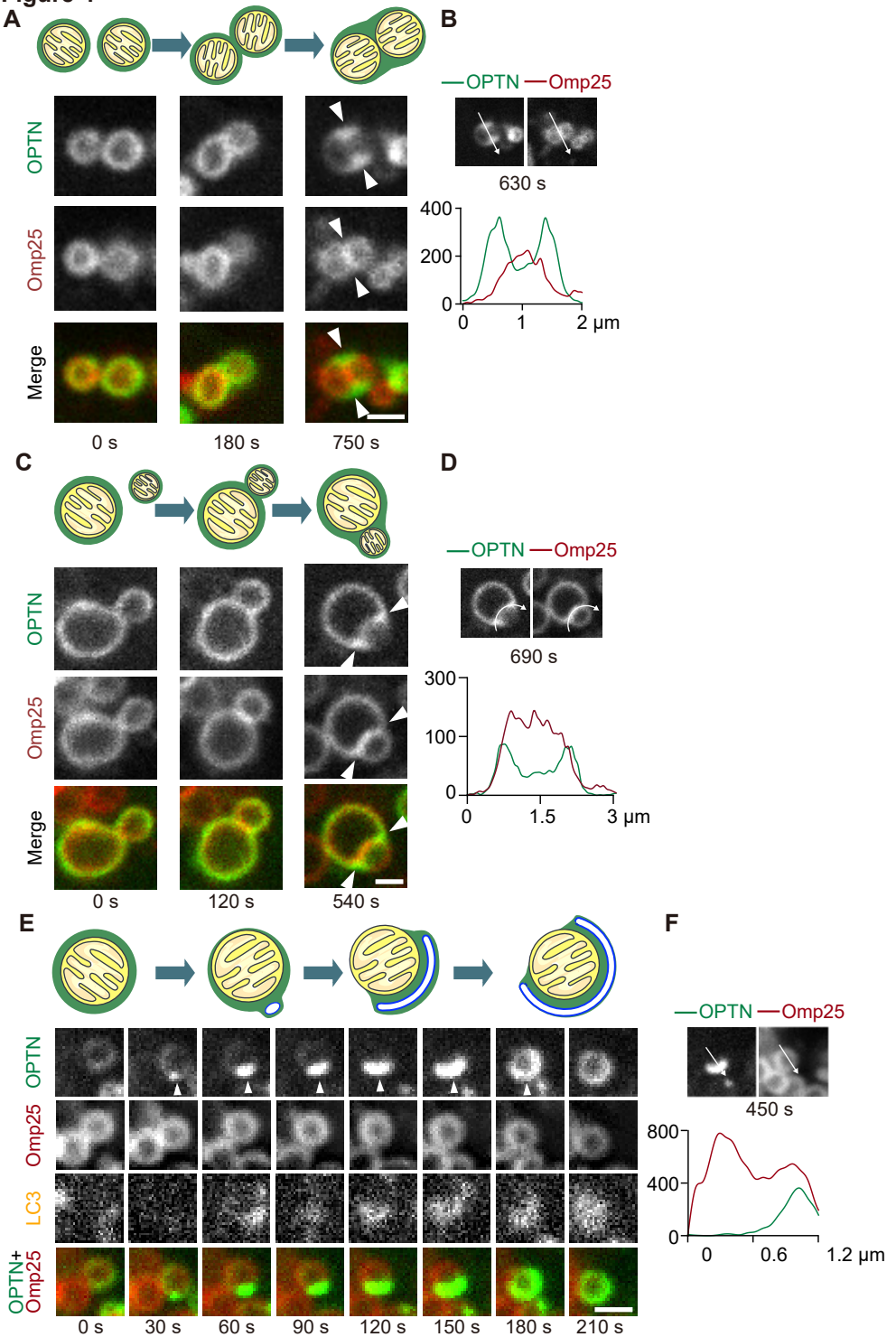

Figure 4. OPTN condensates redistribute upon contact with membranes.
(A–D) Time-lapse images (A and C) and spline graphs (B and D) of two separate mitochondria approaching and contacting each other. Events of the attachment of two mitochondria with comparable sizes (A and B) and with differing sizes (C and D) were observed. The line graphs represent the intensity profiles along the indicated lines in the respective images shown (B and D). The arrowheads indicate redistributed OPTN signals filling the cleft between two adjacent mitochondria. Scale bars indicate 1 µm. See also Movie EV1 for the time-lapse video corresponding to (C).
(E and F) Time-lapse images (E) and a spline graph (F) of a mitochondrion with an isolation membrane elongating on its surface. The arrowhead indicates the elongating isolation membrane. The line graph represent the intensity profiles along the indicated lines in the respective images shown. Scale bars indicate 1 µm. See also Movie EV2 for the time-lapse video corresponding to (E).

Figure 5

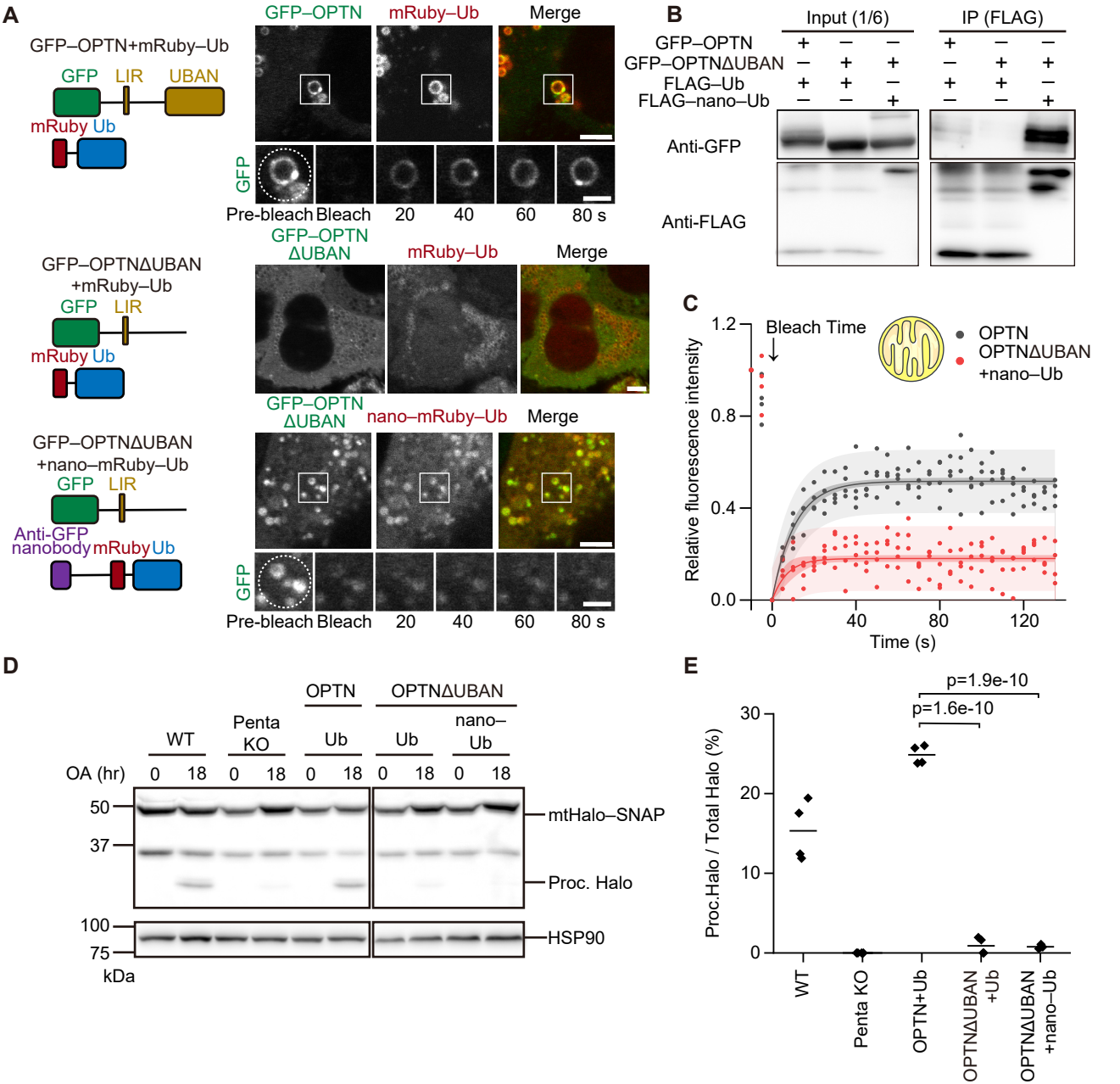

Figure 5. Liquid-like property of OPTN condensates is required for mitophagy.
(A) HeLa cells lacking all five autophagy adaptors (penta KO cells) expressing both GPF–OPTN and mRuby–Ub (top), both GFP–OPTNΔUBAN and mRuby–Ub (middle), or both GFP–OPTNΔUBAN and anti-GFP nanobody–mRuby–Ub (bottom) at 45 min after 20 μM CCCP treatment. Time-lapse images of GFP FRAP are shown. Photobleached areas are circled by dotted lines. Scale bars indicate 4 μm and 2 μm (magnified images).
(B) Interaction between GFP–OPTN mutants and FLAG–Ub or FLAG–nanobody–Ub was investigated by immunoprecipitation with an anti-FLAG antibody and immunoblotting with an anti-GFP antibody.
(C) Quantification of GFP FRAP on separate mitochondria (Mt) in penta KO cells expressing both GFP–OPTN and mRuby–Ub or both GFP–OPTNΔUBAN and anti-GFP nanobody–mRuby–Ub at 45 min after 20 μM CCCP treatment. Data were collected from four structures and were fitted to the equation y = a*(1 − exp(−b*x)). The dark shading represent the 95% confidence intervals, and the light shading represent the 95% prediction intervals.
(D and E) Representative data (D) and quantification (E) of HaloTag (Halo) processing assay using cells expressing the indicated OPTN and Ub constructs. Cells expressing the mtHalo–SNAP mitophagy reporter were treated without (0 h) and with 1 μM oligomycin and 2 μM antimycin for 18 h. The amount of processed Halo (proc. Halo) indicates the relative amount of mitochondria degraded by the lysosomes. Solid horizontal bars indicate the means, and dots indicate the data from four independent experiments. Differences were statistically analyzed by one-way analysis of variance with Dunnett' s post-hoc test.

Figure 6

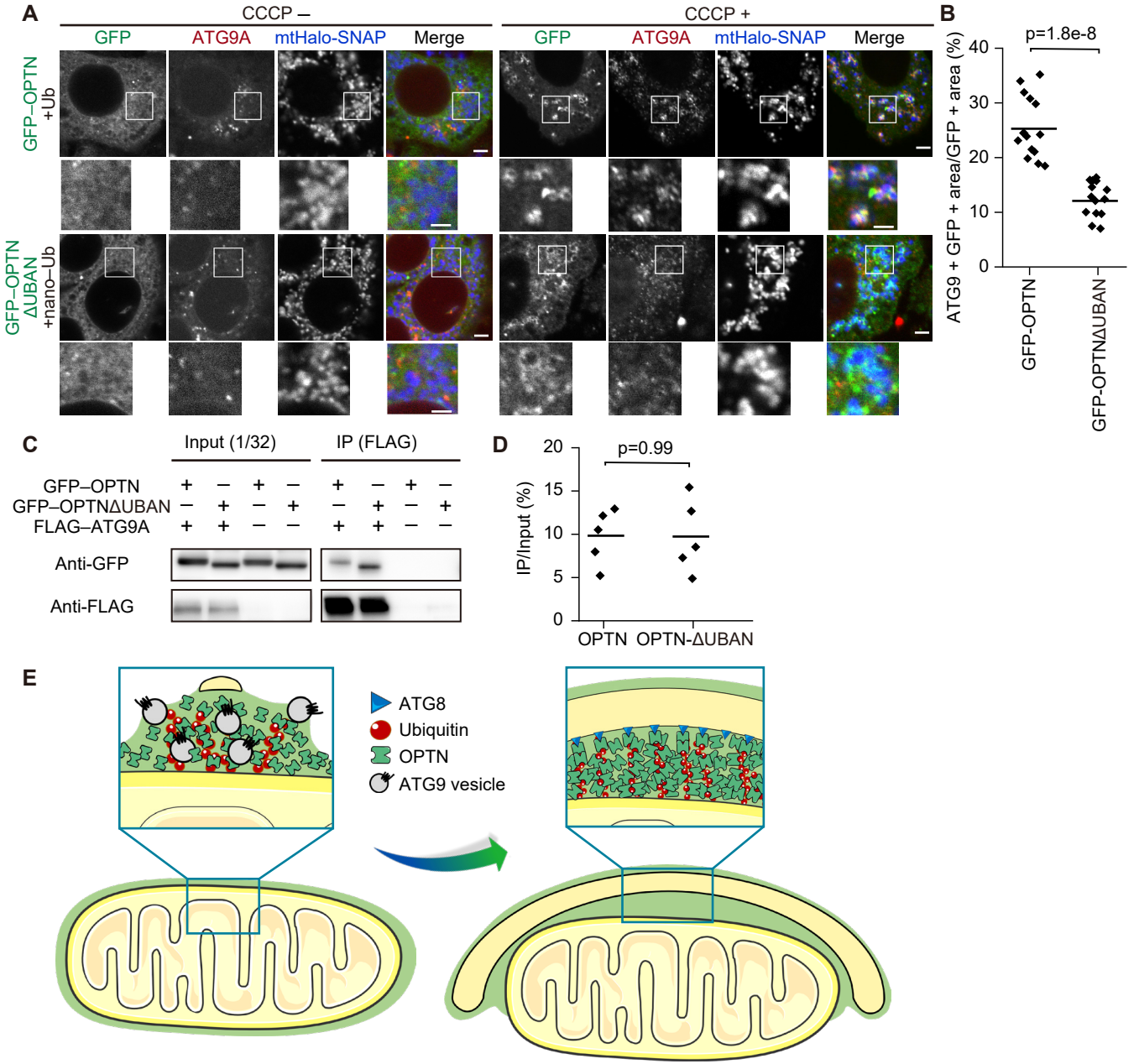

Figure 6. Liquid-like property of OPTN condensates is required for the recruitment of ATG9A vesicles.
(A and B) Localization of ATG9 vesicles under normal (CCCP−) or mitophagy-inducing conditions (CCCP+, 60 min) (A) and quantification (B) of ATG9A colocalization with mitochondria. Endogenous ATG9 was immunostained in penta KO cells expressing both GFP–OPTN and mRuby–Ub or both GFP–OPTNΔUBAN and mRuby–nanobody–Ub together with mitochondrially targeted Halo–SNAP (mtHalo–SNAP). Scale bars indicate 4 μm and 2 μm (magnified images). Solid horizontal bars indicate the means, each dot indicates the mean value from one field of view with ≥10 cells (n=15). Differences were statistically analyzed by one-way analysis of variance with Dunnett' s post-hoc test.
(C and D) Representative data (C) and quantification (D) of organelle immunoprecipitation in cells expressing GFP–OPTN or GFP–OPTNΔUBAN in the presence or absence of FLAG-ATG9A. ATG9 vesicles were immunoprecipitated by FLAG M2 beads and GFP was blotted to detect the interaction between GFP–OPTN (WT or ΔUBAN) and ATG9 vesicles at 60 min after 20 μM CCCP treatment. Solid horizontal bars indicate the means, and dots indicate the data from five independent experiments. Differences were statistically analyzed by one-way analysis of variance with Dunnett' s post-hoc test.
(E) The models of ATG9 vesicle recruitment (left) and isolation membrane elongation (right) mediated by liquid-like OPTN condensates. Partial or complete wetting of phase-separated OPTN enables the recruitment of ATG9 vesicles to ubiquitinated mitochondria (left). Wetting of OPTN on mitochondria and isolation membranes also facilitates the engulfment of mitochondria by the isolation membranes (right).

Figure EV1

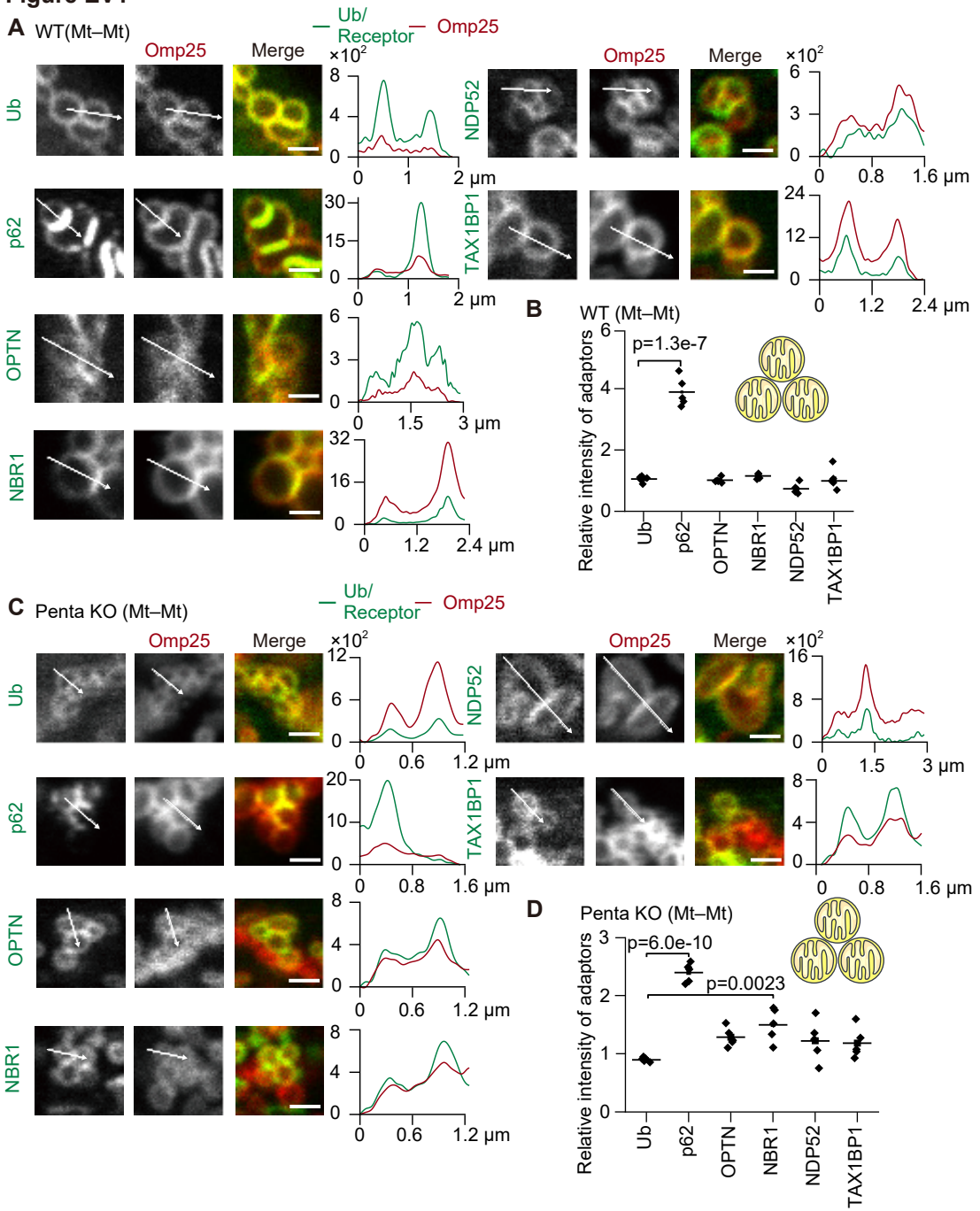

Figure EV1. Localization of autophagy adaptors between mitochondria during Parkin-mediated mitophagy.
(A and C) Representative images (left) and spline graphs of the intensity profiles along the indicated lines (right) of wild-type HeLa cells (A) or penta KO cells (C) expressing one of the GFP–tagged autophagy adaptors or ubiquitin and mRuby–Omp25 at 45 min after 20 μM CCCP treatment. The Y axis in the graphs indicates the fluorescence intensity.
(B and D) The relative intensity of each adaptor was calculated as in Figure 1C. Solid bars indicate the means and dots indicate the data from 5 structures. Differences were statistically analyzed by one-way ANOVA with Dunnett' s post hoc test.